Fully-stripped-beryllium-ion collisions with $2\ell m$ states of atomic hydrogen: Total and state-selective electron-capture cross sections

N. W. Antonio [1,*] C. T. Plowman [1] I. B. Abdurakhmanov [2] I. Bray [1] and A. S. Kadyrov [1,†]

[1]*Department of Physics and Astronomy and Curtin Institute for Computation,*
Curtin University, GPO Box U1987, Perth, Western Australia 6845, Australia
[2]*Pawsey Supercomputing Research Centre, 1 Bryce Avenue, Kensington, Western Australia 6151, Australia*

Integrated total and state-selective electron-capture cross sections are calculated for bare beryllium ion scattering on atomic hydrogen initially configured in the $2\ell m$ states (where $n = 2$, ℓ, and m are the principal, angular momentum, and magnetic quantum numbers, respectively). This is done using the wave-packet convergent close-coupling approach which solves the three-body Schrödinger equation by employing a two-center expansion for the total scattering wave function. These calculations are performed within a projectile-energy range of 1 to 500 keV/u. The results suggest that at low energies, collisions with hydrogen in each of the $2\ell m$ states produce a total electron-capture cross section approximately an order of magnitude larger than for scattering on the ground state. However, as projectile energy increases, the cross section for capture from the excited states falls well below the H($1s$) electron capture cross section. A possible reason for this observation could be related with the way the target electron radial densities are distributed in different initial states. The results obtained in this work are compared to previous calculations where available. In terms of the n-resolved charge-exchange cross sections, significant disagreement is found between our results and some preceding calculations available in the literature to warrant further investigations.

I. INTRODUCTION

The study of bare beryllium ion collisions with atomic hydrogen plays an important role in plasma diagnostics and heating [1]. Major fusion projects such as the International Thermonuclear Experimental Reactor (ITER) and the Joint European Torus (JET) intend to use beryllium-containing materials inside plasma-facing components [2,3]. High temperatures required inside these reactors lead to erosion of Be atoms from the wall into the plasma that can then become fully ionized to form Be^{4+} ions. How these impurity ions affect properties such as the temperature and density of the plasma can be understood through the charge-exchange recombination spectroscopy (CXRS) technique [4]. When a neutral hydrogen beam is injected into the reactor, collisions involving Be^{4+} ions and atomic hydrogen can occur. These may lead to charge-exchange processes that produce excited Be^{3+} ions. The resulting hydrogen-like ions emit photons via the de-excitation process, which can be detected and used to diagnose the aforementioned properties of the plasma. Initially, hydrogen atoms composing the neutral beam injected into the reactor are in the ground state; however, it is expected that as the beam penetrates, a fraction of the atoms become excited. It has been shown that despite possibly low fractions of excited hydrogen present in the beam, charge exchange cross sections for impurity ions colliding with H($2s$, $2p_0$, $2p_1$) are

expected to be at least an order of magnitude larger than that for collisions with H($1s$) [5]. For this reason, contributions to formation of the Be^{3+} ions in the reactor due to scattering on excited hydrogen atoms cannot be neglected.

Generally, a number of distinct theoretical methods exist for ion-atom collisions in the energy region of interest. These are the first-order perturbation approach with corrected boundary conditions (B1B) [6], the continuum distorted-wave (CDW) approach [7], the classical trajectory Monte Carlo (CTMC) method [8,9], the semiclassical two-center atomic-orbital close-coupling (TC-AOCC) approach [10,11], the two-center basis-generator method (TC-BGM) [12], the molecular orbital close-coupling (MOCC) approach [13,14], and the lattice approach [15,16]. Two most recent reviews of the field of ion-atom collisions were given in Refs. [17,18]. Some of these methods have been applied to Be^{4+} collisions with H($1s$) [6,9,10,13,15,16]. However, scattering calculations involving excited states are scarce.

We have studied collisions between the Be^{4+} ions and ground-state atomic hydrogen in previous work [19]. Here, we extend this research to bare beryllium ion scattering on hydrogen in its lowest excited states within the projectile-energy domain between 1 and 500 keV/u. Specifically, this includes collisions with the hydrogen target initially in the $2s$, $2p_0$, and $2p_1$ states. The focus is to study electron capture (EC) processes. In the excited state, the electron is bound weaker to the target nucleus in comparison to the ground state. Therefore, given the strong Coulomb attraction to the Be^{4+} projectile, processes such as electron capture, ionization, and target excitation are much more likely to occur in the low to

*nicholas.antonio@student.curtin.edu.au
†a.kadyrov@curtin.edu.au

intermediate incident energy regime in comparison to collisions with H(1s). This introduces further complications as a larger number of final asymptotic channels become accessible. Thus, thorough investigation is required to establish the required number of basis states on both centers to be able to calculate the total integrated and state-selective electron-capture cross sections sufficiently accurately.

Due to the toxicity of beryllium, there exist no experimental data for comparison. However, within the considered energy region, there have been a number of theoretical results obtained using the methods mentioned above. These include the CTMC [20–22], MOCC [14,23], and AOCC [24,25] calculations and applications of the numerical grid approach to solving the time-dependent Schrödinger equation for the total scattering wave function (GTDSE) [20]. The CTMC method is a statistical approach built using a classical mechanics framework. Given its statistical nature, this method relies on a large set of collision simulations to calculate any desired integrated cross sections. The AOCC method used in Refs. [24,25] is a semiclassical approach, whereby the projectile is considered to have a well-defined trajectory while electron dynamics is treated fully quantum mechanically. From these considerations, the total scattering wave function is represented as an expansion of atomic states on both the target and projectile centers. This method has a number of common features to our method; however, as described below, the results differ substantially. The MOCC method used in Refs. [14,23] follows a closely related scheme; however, the total scattering wave function is expanded in terms of molecular states. The accuracy of these two approaches relies on the number and type of basis states used in the expansion. Also, by design the MOCC method is valid within the low incident energy regime, whereas the AOCC method is applicable in the intermediate to high energy domains. The GTDSE method [20] encases the target and projectile within a three-dimensional lattice, for which the time-dependent Schrödinger equation for the total scattering wave function is solved numerically at each node in the lattice. The limitation of this approach is the need for considerable memory allocations to store large 3D lattices. The method is accurate in the intermediate energy region; however, it has only been applied to the H(2s) state and only at two energies: 20 and 100 keV/u.

Considering the target initially in the 2s state, CTMC results by Ziaeian and Tökési [21] display large discrepancies compared to AOCC calculations by Igenbergs [25] in the total EC cross section at energies greater than 60 keV/u. The same observation was made when configuring the target initially in the various 2p states. This is an intriguing result as in the past the CTMC and AOCC methods have been shown to generally agree in the intermediate to high energy regime in terms of the total EC cross section [19]. Again considering the hydrogen target initially in the 2s state, it is found that two sets of MOCC calculations by Errea *et al.* [14] and Shimakura *et al.* [23] contradict each other in the n-partial EC cross section and consequently also in the total EC cross section at projectile energies between 1 to 10 keV/u. The reason for this considerable difference in the results is yet to be understood. Disagreement is also found when comparing the n- and $n\ell$-partial EC cross sections for Be^{4+}-H(2s) collisions at 100 keV/u, with the two available sets of results using the

AOCC approach [25] and the GTDSE method [20]. The majority of the work done on this system in the past has focused on obtaining cross sections with the target initially in the 2s state. Hoekstra *et al.* [22] reported results by statistically averaging over all $n = 2$ states. Hence, work done on the total and state-selective EC cross sections for collisions with hydrogen in the 2p_0 and 2p_1 states is limited. Furthermore, many of the calculations conducted for state-selective EC processes have focused on obtaining accurate n-partial cross sections. It is known, however, that the $n\ell$-partial EC cross sections are also of particular importance for plasma impurity diagnostics. Therefore, further work on obtaining accurate $n\ell$-resolved cross sections is required.

In this study, we consider bare beryllium ion scattering on atomic hydrogen in all 2ℓm states. To this end, we employ the semiclassical two-center wave-packet convergent close-coupling (WP-CCC) approach first presented in Refs. [26,27]. This approach expands the total scattering wave function using a basis composed of bound and pseudo-continuum states around the two centers to describe all asymptotic channels. The continuum pseudostates are constructed from wave packets that represent ionization of the electron into discrete energy bins. The method has been applied to scattering systems such as proton-hydrogen [28] and bare multiply charged ion-hydrogen [29–31] collisions along with proton collisions with multielectron targets [32,33]. The WP-CCC method has also been used to study proton collisions with atomic hydrogen initially in the various 2ℓm states [34]. It was found that a much larger basis is required in comparison to proton scattering on ground-state hydrogen in order to obtain converged results. In this paper, we present calculations for total and n- and $n\ell$-resolved electron-capture cross sections using the WP-CCC formalism within the projectile energy range of 1 to 500 keV/u and compare our results to previous works.

This paper is set out as follows. In Sec. II, a brief overview of the WP-CCC formalism is given. The results of the calculations are presented in Sec. III. Lastly, in Sec. IV, conclusions from this investigation are drawn. Atomic units (a.u.) are used throughout this paper unless otherwise stated.

II. TWO-CENTER WAVE-PACKET CONVERGENT CLOSE-COUPLING APPROACH

A full description of the WP-CCC approach to ion-atom collisions is provided in Refs. [26,27]. Here we present a brief summary of the formalism to treat bare beryllium ion collisions with excited atomic hydrogen. This is a three-body scattering problem. We use Jacobi coordinates. In this implementation, a semiclassical approach is used whereby the projectile nucleus is assumed to have a well-defined trajectory. The target hydrogen atom is located at a fixed origin such that the trajectory of the projectile can be expressed by $\boldsymbol{R} = \boldsymbol{b} + \boldsymbol{v}t$, where $\boldsymbol{b}$ is the impact parameter, $\boldsymbol{v}$ is the projectile velocity, and t is time. The z component for the position of the projectile is $\boldsymbol{v}t$. Before the collision, $t = -\infty$ such that $t = 0$ corresponds to the distance of the closest approach for the projectile.

In the energy regime considered in this work, the collision system is described by the nonrelativistic Schrödinger
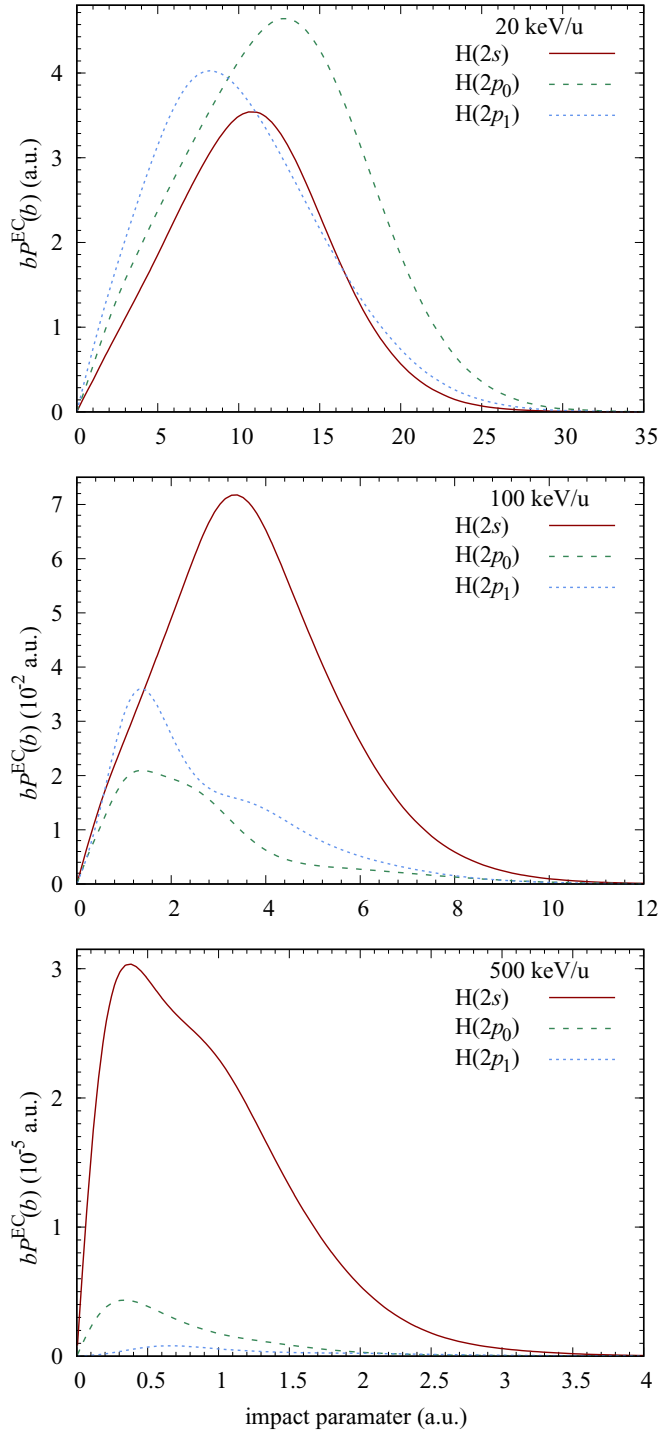
FIG. 1. The weighted probability distributions for total electron capture in Be^{4+} collisions with H($2s$), H($2p_0$), and H($2p_1$) at projectile energies 20, 100, and 500 keV/u.

equation for the total scattering wave function Ψ_i^+ as

$$(H - E)\Psi_i^+ = 0. \tag{1}$$

Here, the solution Ψ_i^+ obeys outgoing wave boundary conditions and the subscript i indicates the initial channel. Also, E is the total energy of the collisional system and H is the total three-body Hamiltonian. We represent the solution to Eq. (1)
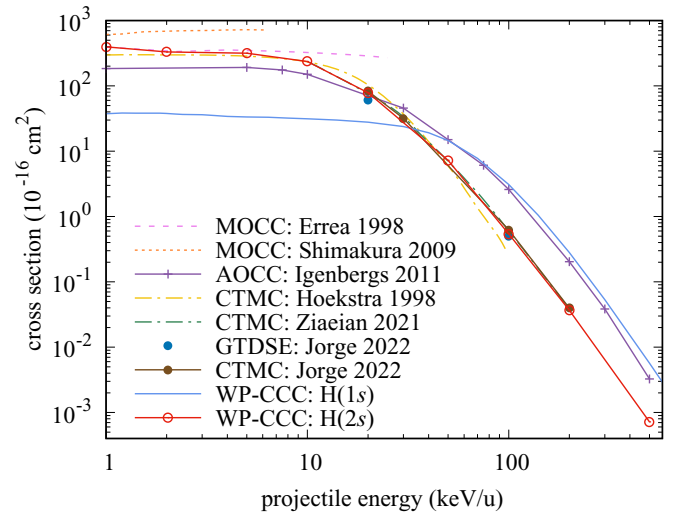

FIG. 2. The total cross section for electron capture in Be^{4+} collisions with atomic hydrogen initially in the $2s$ state: The present WP-CCC results are shown alongside previous calculations by Errea *et al.* [14] and Shimakura *et al.* [23] using the MOCC method, Igenbergs [25] with the AOCC approach, Hoekstra *et al.* [22] and Ziaeian and Tökési [21] using the CTMC method, and Jorge *et al.* [20] with the GTDSE and CTMC approaches. The WP-CCC results for H($1s$) are also shown.

as an expansion in terms of all asymptotic channels, i.e.,

$$\Psi_i^+ \approx \sum_{\alpha=1}^{N} F_\alpha(t, \boldsymbol{b}) \psi_\alpha(\boldsymbol{r}_T) e^{i\boldsymbol{k}_\alpha \cdot \boldsymbol{\sigma}_T} + \sum_{\beta=1}^{M} G_\beta(t, \boldsymbol{b}) \psi_\beta(\boldsymbol{r}_P) e^{i\boldsymbol{k}_\beta \cdot \boldsymbol{\sigma}_P}, \tag{2}$$

where the summation indices α and β denote the final target and projectile electronic states as a result of the collision. The vectors $\boldsymbol{r}_T$ and $\boldsymbol{r}_P$ are the positions of the electron relative to the target and projectile nuclei, respectively. The position

FIG. 3. The total cross section for electron capture in Be^{4+}-H($2p_0$) collisions: the present WP-CCC results are shown alongside previous calculations by Igenbergs [25] with the AOCC approach and Ziaeian and Tökési [21] using the CTMC method. The WP-CCC results for H($1s$) are also shown.
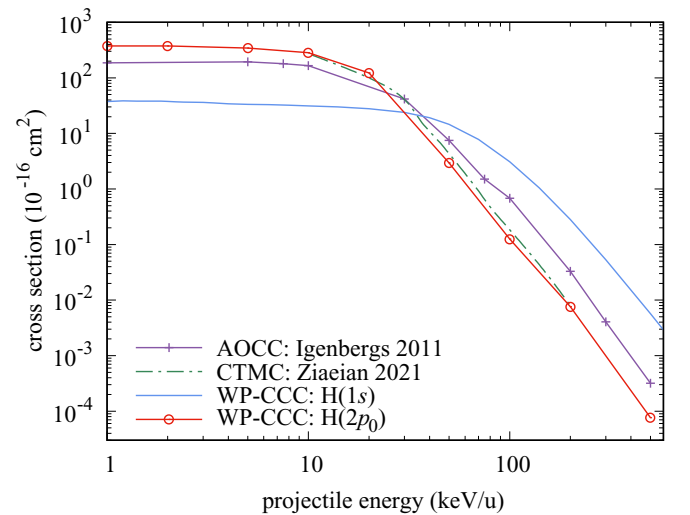
FIG. 4. The total cross section for electron capture for Be^{4+}-H($2p_1$) collisions: The present WP-CCC results are shown alongside previous calculations by Igenbergs [25] with the AOCC approach and Ziaeian and Tökési [21] using the CTMC method. The WP-CCC results for H($1s$) are also shown.
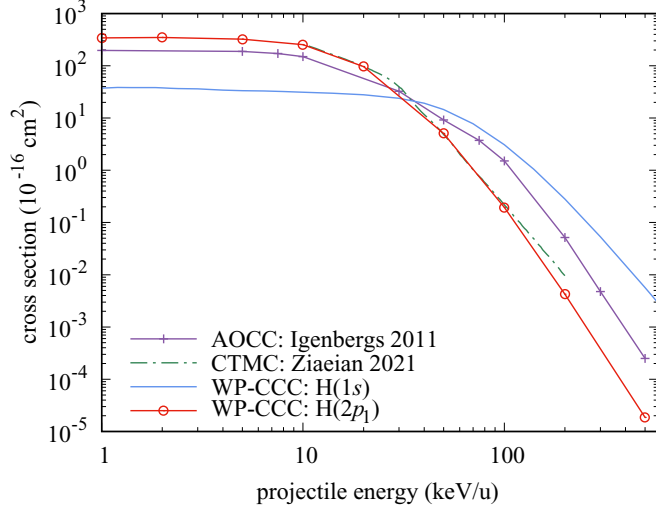
of the projectile nucleus relative to the center of mass of the target is $\boldsymbol{\sigma}_T$ while the position of the center of mass of the projectile-electron pair relative to the target nucleus is $\boldsymbol{\sigma}_P$. The vector $\boldsymbol{k}_\alpha$ represents the relative momentum between the projectile and target atom in the channel α. Similarly, $\boldsymbol{k}_\beta$ is the relative momentum between the target nucleus and formed projectile atom as a result of electron capture into the state β. The basis for this expansion consists of both N target-centered and M projectile-centered states denoted by ψ_α and ψ_β, respectively. After the collision, i.e., as $t \rightarrow +\infty$, the unknown expansion coefficients F_α and G_β represent the probability amplitudes for transitions into the final target and projectile states α and β, respectively. For more discussion, see Refs. [27].

Both sets of states $\{\psi_\alpha\}_N$ and $\{\psi_\beta\}_M$ are broken into two subsets, one to describe bound states on each center and the other to represent the continuum. In this approach, true negative-energy eigenstates are used to describe the bound states on each center. To construct positive-energy pseudostates, we subdivide the continuum into a number of energy bins. This discretization procedure is performed up to some maximum electron energy $\varepsilon_{\max}$. In momentum space, this gives a set of bins $[k_{n-1}, k_n]_{n=1}^{N_c}$, where N_c is the number of bins used to discretize the continuum. Note that $k_0 = 0$ and $k_{N_c} = k_{\max}$. Using these definitions, we define the radial component for the nth wave packet (WP) pseudostate on each center by

$$\phi_{n\ell}^{\text{WP}}(r) = \frac{1}{\sqrt{w_n}} \int_{k_{n-1}}^{k_n} U_\ell^Z(r, k) dk. \quad (3)$$

Here, $w_n = k_n - k_{n-1}$ is the width of the nth bin, Z is the charge of either the target or projectile nucleus, and $U_\ell^Z(r, k)$ is the standard Coulomb wave. The angular components of the WP pseudostates are given by spherical harmonics. The ejected electron energy for the nth WP pseudostate is given by
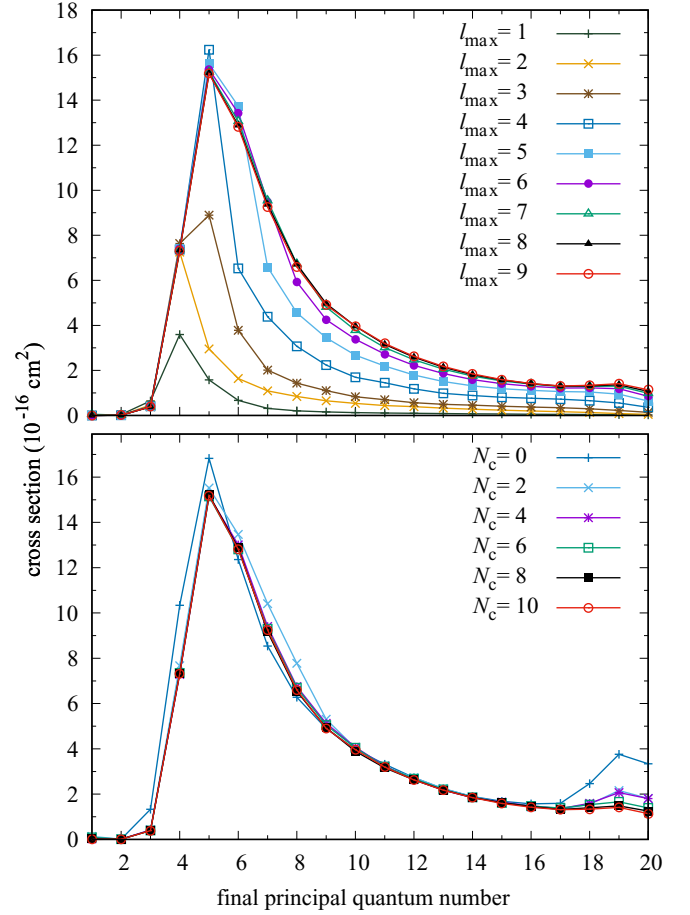

FIG. 5. n-partial electron-capture cross sections for Be^{4+}-H($2s$) collisions at projectile energy of 20 keV/u: convergence of the WP-CCC results with respect to $\ell_{\max}$ (top panel) and N_c (bottom panel) of the basis states included in the expansion.

$\epsilon_n = (k_n^2 + k_n k_{n-1} + k_{n-1}^2)/6$. In summary, this approach uses true negative-energy eigenstates and WP pseudostates around each center for the expansion in Eq. (2). It is worth noting that the set of states used to describe each center individually are all orthogonal to one another. However, the basis functions from one center are not necessarily orthogonal to the basis functions about the other center. For an in-depth analysis and justification for the implementation of wave-packet pseudostates in our approach, please refer to Refs. [26,27].

In order to calculate the transition amplitudes for various processes, the unknown expansion coefficients F_α and G_β must be known in the asymptotic region ($t \rightarrow +\infty$). To this end, by substituting the expansion (2) of the total scattering wave function Ψ_i^+ into Eq. (1), we get a system of first-order differential equations for the time-dependent expansion coefficients

$$i\dot{F}_{\alpha'} + i\sum_{\beta=1}^{M} \dot{G}_\beta \tilde{K}_{\alpha'\beta} = \sum_{\alpha=1}^{N} F_\alpha D_{\alpha'\alpha} + \sum_{\beta=1}^{M} G_\beta \tilde{Q}_{\alpha'\beta},$$

$$i\sum_{\alpha=1}^{N} \dot{F}_\alpha K_{\beta'\alpha} + i\dot{G}_{\beta'} = \sum_{\alpha=1}^{N} F_\alpha Q_{\beta'\alpha} + \sum_{\beta=1}^{M} G_\beta \tilde{D}_{\beta'\beta},$$

$$\alpha' = 1, 2, \ldots, N, \quad \beta' = 1, 2, \ldots, M. \quad (4)$$

FIG. 6. *n*-partial electron-capture cross sections for Be^{4+}-H($2p_0$) collisions at projectile energy of 20 keV/u: convergence of the WP-CCC results with respect to ℓ_{max} (top panel) and N_c (bottom panel) of the basis states included in the expansion.
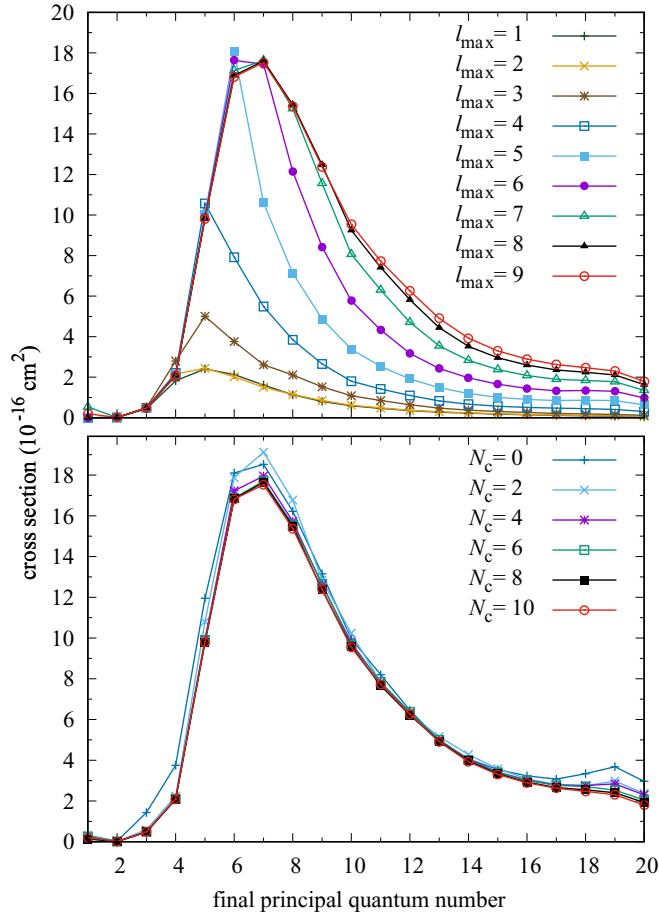

FIG. 7. *n*-partial electron-capture cross sections for Be^{4+}-H($2p_1$) collisions at projectile energy of 20 keV/u: convergence of the WP-CCC results with respect to ℓ_{max} (top panel) and N_c (bottom panel) of the basis states included in the expansion.

Dots over F_α and G_β indicate time derivatives. The quantities $D_{\alpha'\alpha}$ and $\tilde{D}_{\beta'\beta}$ are known as the direct-scattering matrix elements. Furthermore, $K_{\beta'\alpha}$, $\tilde{K}_{\alpha'\beta}$, $Q_{\beta'\alpha}$, and $\tilde{Q}_{\alpha'\beta}$ are the overlap and electron exchange matrix elements, respectively. For further details regarding the forms of the scattering matrix elements, see Ref. [19]. As described in Ref. [35], the direct matrix elements are calculated in spherical coordinates whereas the overlap and electron-transfer matrix elements are evaluated in prolate spheroidal coordinates.

The close-coupling equations (4) are subject to the following initial state boundary condition

$$F_\alpha(t = -\infty, \boldsymbol{b}) = \delta_{\alpha i}, \quad \alpha = 1, 2, \ldots, N, \quad (5)$$

$$G_\beta(t = -\infty, \boldsymbol{b}) = 0, \quad \beta = 1, 2, \ldots, M, \quad (6)$$

where subscript i is the label for the initial state of the hydrogen target. Upon solving for F_α and G_β and taking $t \to +\infty$, the fully state-resolved integrated direct-scattering (DS) and electron-capture cross sections can be calculated [19]. To obtain $n\ell$ partial cross sections for either DS or EC processes, the set of fully state-resolved cross sections for transitions into states with the same n and ℓ quantum numbers are summed over the magnetic quantum number m. Similarly, we sum over
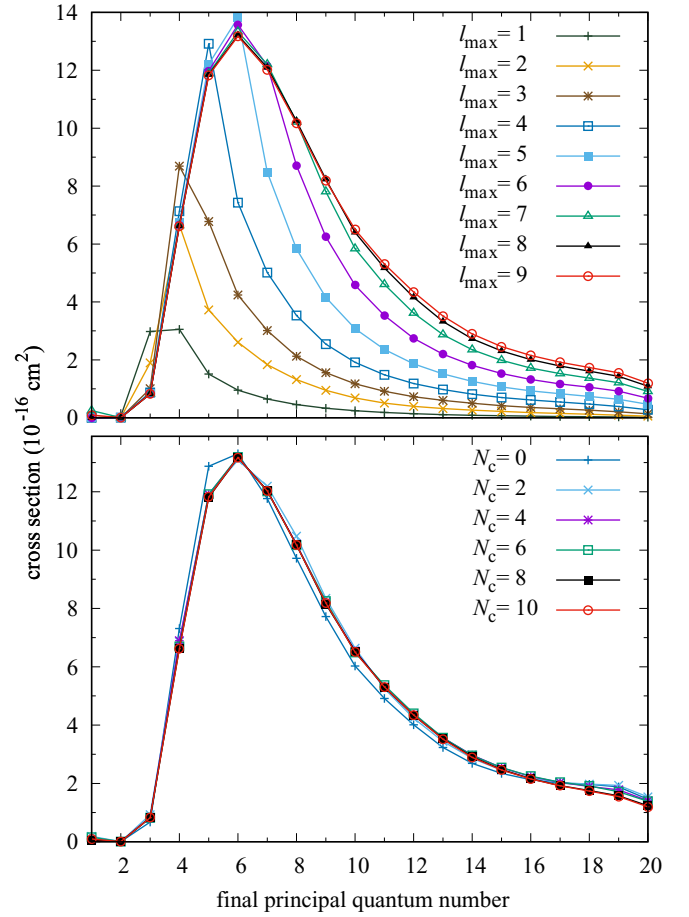
the angular momentum quantum number to obtain *n*-resolved cross sections.

III. RESULTS AND DISCUSSION

In this section, we begin with an overview of the details of our calculations. Then we present our results for the total electron-capture (TEC) cross sections for various initial states. Then, the results for state-selective EC cross sections will be presented. Comparisons to preceding theoretical studies will be made throughout this paper where possible. In this work, we consider the hydrogen target initially in the 2*s*, 2*p*$_0$, and 2*p*$_1$ states. It is worth mentioning that all cross sections we obtain for scattering on H(2*p*$_1$) are applicable also for H(2*p*$_{-1}$) as they do not depend on the sign of the magnetic quantum number. Hence, any reference to scattering on atomic hydrogen initially in the 2*p*$_1$ state should also be seen as equivalent to collisions with H(2*p*$_{-1}$).

A. Details of calculations

To solve the close-coupling equations (4) for the set of expansion coefficients, we employ the Runge-Kutta technique along a *z*-grid within the range $[-z_{max}, +z_{max}]$ and denser
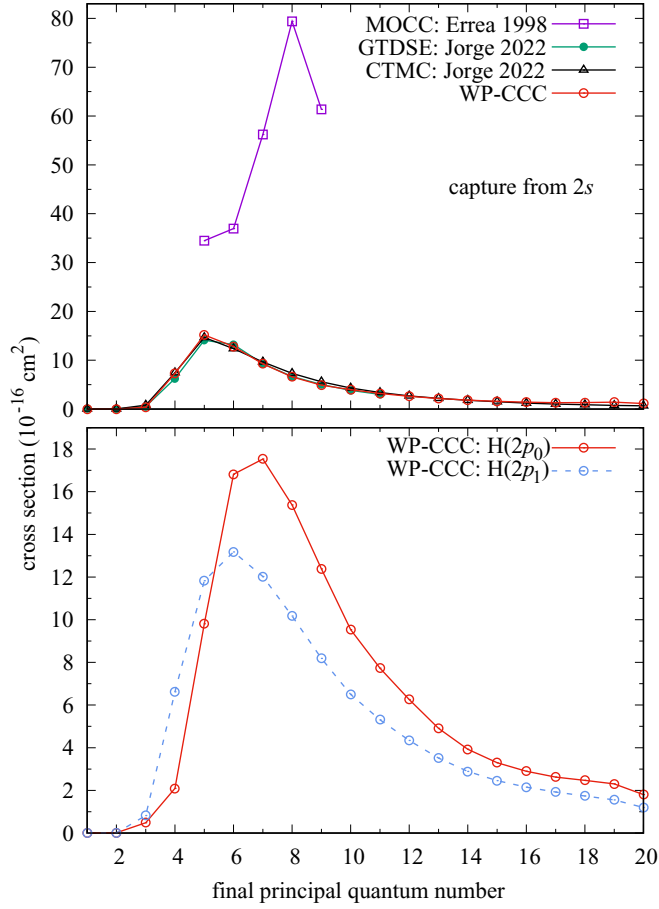
FIG. 8. *n*-partial electron-capture cross sections for Be^{4+} scattering on H(2s) (top panel) and H($2p_0$) and H($2p_1$) (bottom panel) at projectile energy of 20 keV/u: The present WP-CCC results for collisions with H(2s) are shown alongside the MOCC calculations made by Errea *et al.* [14] and results by Jorge *et al.* [20] using the GTDSE and CTMC approaches.

FIG. 9. *n*-partial electron-capture cross sections for Be^{4+}-H(2s) collisions at projectile energy of 100 keV/u: convergence of the WP-CCC results with respect to ℓ_{max} (top panel) and N_c (bottom panel) of the basis states included in the expansion.

discretization around 0. In terms of the structure of this grid, the important parameters to consider are z_{max} (the magnitude of the grid boundaries) and also the number of points within the region. In this work, we find that the difference between setting $z_{max} = 125$ a.u. and $z_{max} = 150$ a.u. gives negligible difference in all cross sections considered. Therefore, we set z_{max} to be 150 a.u. for all calculations. However, at low impact energies, we find a larger number of time steps is required in comparison to high projectile energies. To this end, we include a maximum of 8000 time steps for the lowest impact energy considered (1 keV/u) in order to obtain accurate results. When increasing projectile energy, this number is systematically decreased down to 1200 points at 500 keV/u. Also, it is checked that the unitarity of the total scattering wave function is preserved to at least three decimal places at every point within the *z*-grid during the Runge-Kutta propagation. Indeed, within the scattering region there exists some overlap between WP pseudostates centered around the target and projectile nuclei. However, as discussed in our preceding paper [19], when calculating the norm of the two-center expansion (2), there is a series of terms that collectively represent the interference between target and projectile centered states. We have observed
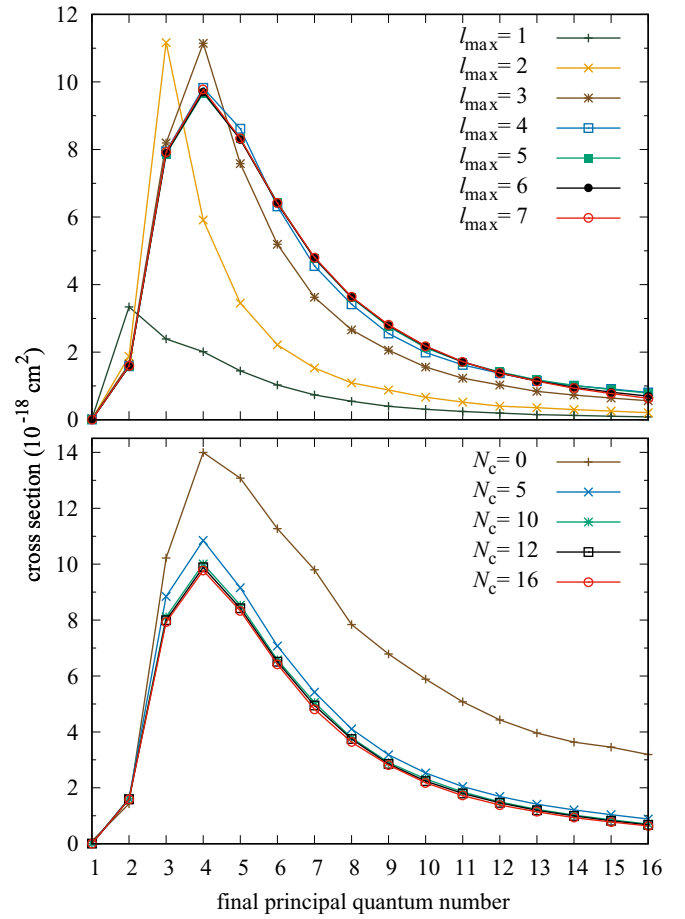
that this nonvanishing overlap between target and projectile centered basis states is essential in preserving unitarity of the total scattering wave function across the entire *z*-grid. Overall, the uncertainty in the calculated cross sections with respect to number of time steps was under 0.5%.

The radial grids used for the integration of the direct matrix elements are extended up to 400 a.u. to obtain reliable results. In constructing the impact parameter mesh, it is found that when looking solely at EC processes the largest impact parameter, b_{max}, needed was 50 a.u. This value for b_{max} is used in the projectile energy range from 1 up to 30 keV/u. Moving toward the upper limit of projectile energy range, it is found that setting $b_{max} = 5$ a.u. is more than sufficient due to sharp fall in the electron-capture probability. Figure 1 shows the weighted total probability distributions for electron capture as functions of impact parameter. The three separate lines correspond to the results for collisions with H(2s), H($2p_0$), and H($2p_1$). The results are shown at three selected energies: 20, 100, and 500 keV/u. From this figure, one can see that as projectile energy increases, the impact parameter corresponding to the maximum of the EC probability distribution reduces. At 20 keV/u, collisions with H($2p_0$) produces the largest TEC cross section, whereas scattering on H(2s) results are the

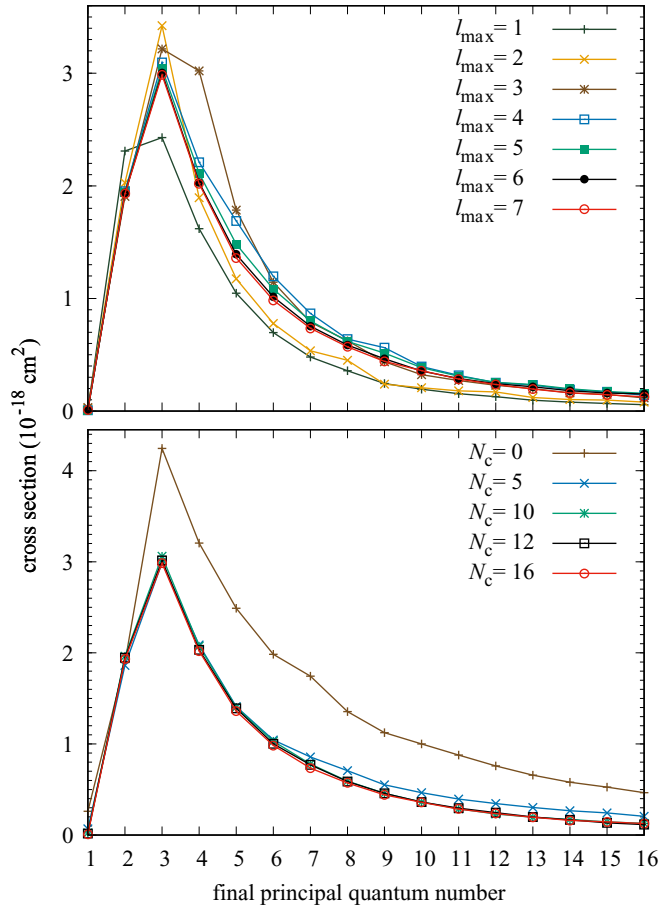FIG. 10. n-partial electron-capture cross sections for Be^{4+}-H($2p_0$) collisions at projectile energy of 100 keV/u: convergence of the WP-CCC results with respect to ℓ_{max} (top panel) and N_c (bottom panel) of the basis states included in the expansion.

FIG. 11. n-partial electron-capture cross sections for Be^{4+}-H($2p_1$) collisions at projectile energy of 100 keV/u: convergence of the WP-CCC results with respect to ℓ_{max} (top panel) and N_c (bottom panel) of the basis states included in the expansion.
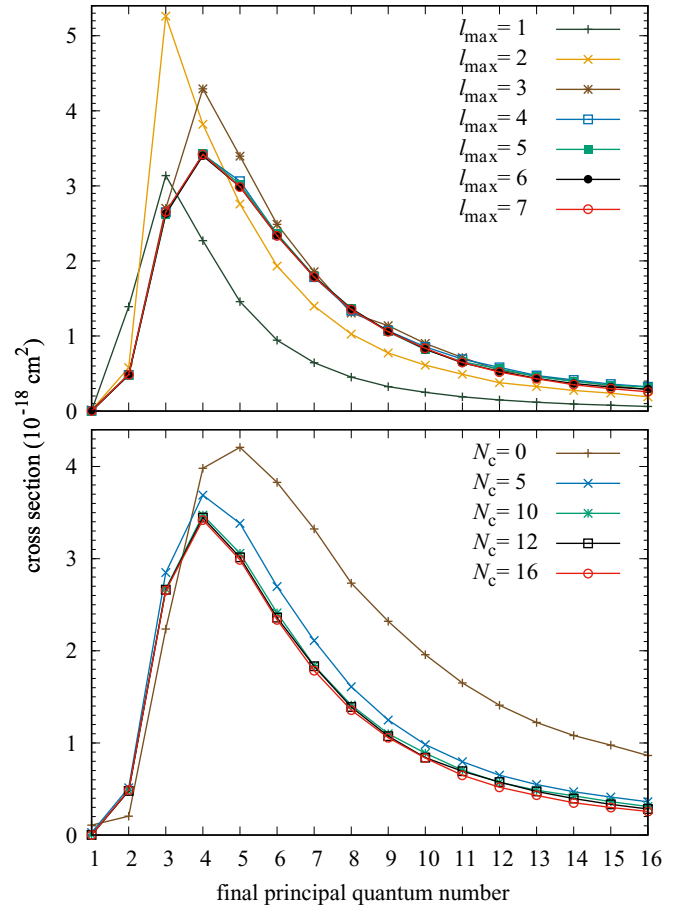
smallest. As the projectile energy increases to 100 keV/u, the TEC cross section dominates for the initial $2s$ state. This is even more pronounced at 500 keV/u.

Following the investigation for suitable z-, radial-, and b-grid parameters, we shift our focus to the size of the basis used in the two-center expansion (2). In all close-coupling-based approaches, the accuracy of the final state-selective and total cross sections depends on the level of convergence reached with respect to the change in basis size. The three variables that characterize the basis are the maximum principal quantum number n_{max}, the maximum orbital quantum number ℓ_{max}, and the number of WP pseudostates N_c. Each of these parameters is systematically increased one at a time, while keeping the others sufficiently high, until an overall convergence on the order of a few percent or better is achieved. We find that when the target is initially in the $n = 2$ states, the number of necessary bound and continuum pseudostates on each center varies dramatically as a function of impact energy. Due to this observation, here we vary the basis size across the energy domain and only include a suitable number of states such that all cross sections of interest to this work are converged at each particular impact energy. The level of convergence in our results with respect to basis size is discussed below in more detail.

B. Total cross sections

Figure 2 displays the energy dependence of the total EC cross section for Be^{4+}-H($2s$) collisions. We begin by comparing the present WP-CCC results with those obtained in our preceding work for Be^{4+}-H($1s$) collisions [19]. We find that in the energy range between 1 and 10 keV/u, the total EC cross section is approximately an order of magnitude larger for Be^{4+}-H($2s$) collisions than for Be^{4+}-H($1s$) collisions. However, for projectile energies >40 keV/u, the situation is opposite. The reason for this is the difference in the radial probability distribution for finding the electron at a certain distance from the target nucleus in the $1s$ and $2s$ states. In the $1s$ state, the electron is most likely to be found closer to the nucleus. At sufficiently high energies, the projectile can approach the target nucleus much closer. This is why we see the total cross section for EC from H($1s$) to be larger in comparison to that from H($2s$) at high projectile energies.

Our calculations are in excellent agreement with the CTMC results by Ziaeian and Tökési [21]. Furthermore, below 10 keV/u we also agree with the MOCC calculations by Errea *et al.* [14]. However, above 10 keV/u the two sets of results deviate, possibly because the energy becomes too high for a MOCC-type approach. The MOCC results by Shimakura
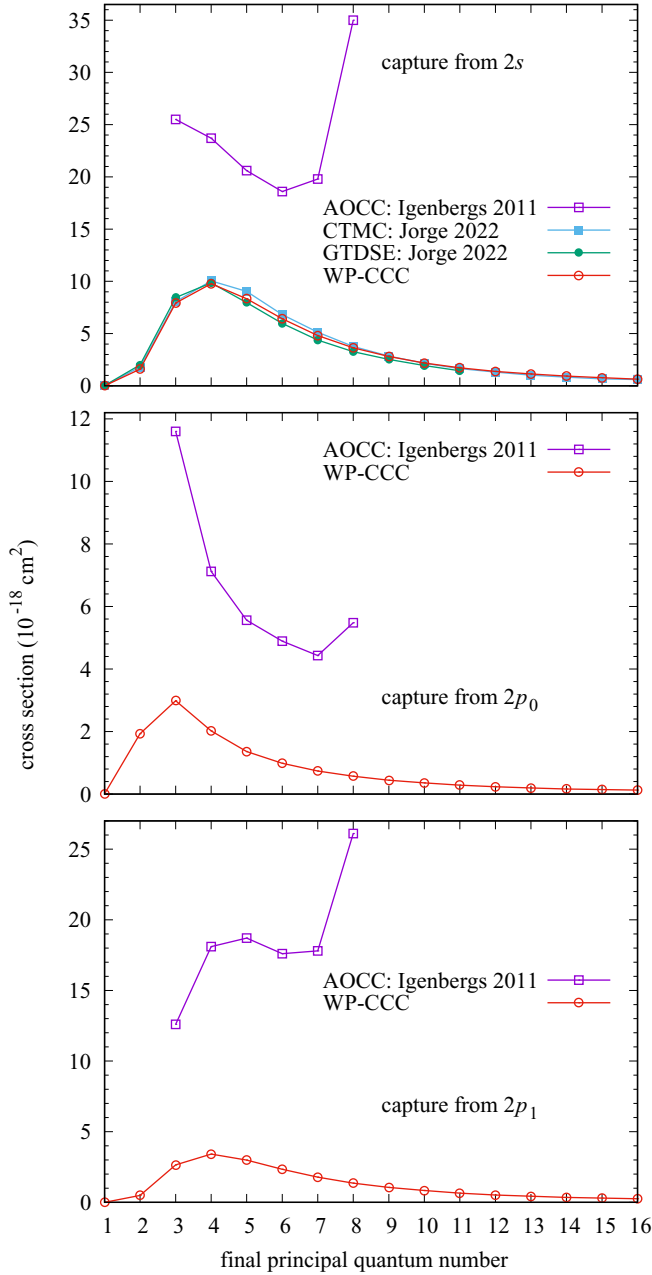
FIG. 12. *n*-partial electron-capture cross sections for Be^{4+} scattering on H(2s) (top panel), H(2p_0) (middle panel), and H(2p_1) (bottom panel) at projectile energy of 100 keV/u: The current WP-CCC results are shown alongside the AOCC calculations by Igenbergs [25] along with the GTDSE and CTMC calculations by Jorge *et al.* [20].

FIG. 13. *n*-partial electron-capture cross sections for Be^{4+}-H(2s) collisions at projectile energy of 500 keV/u: convergence of the WP-CCC results with respect to $\ell_{\max}$ (top panel) and N_c (bottom panel) of the basis states included in the expansion.

CTMC and GTDSE calculations by Jorge *et al.* [20] at the projectile energies 20 and 200 keV/u.

The total EC cross sections for scattering on H(2p_0) and H(2p_1) as functions of projectile energy are displayed in Figs. 3 and 4, respectively. The WP-CCC results are shown alongside the AOCC [25] and CTMC [21] calculations. Just as was the case for the 2s state, we find notable disagreements with the AOCC approach for both 2p_0 and 2p_1 states. Also, the WP-CCC TEC cross sections display good agreement with the CTMC ones.

C. *n*-resolved cross sections

In this section, the calculated *n*-partial EC cross sections will be presented. We also discuss the level of convergence reached in our results with respect to change in basis size. All *n*-partial EC cross sections given below will be shown using points at each final principal quantum number of the formed Be^{3+} atom. These results are connected by lines to guide the eye of the reader.

Figures 5–7 display the dependence on $\ell_{\max}$ and N_c for the *n*-partial EC cross sections for collisions with H(2s), H(2p_0), and H(2p_1), respectively. These results are obtained at an impact energy of 20 keV/u with $n_{\max} = 20$. To start with, we investigate the variation in the results with change in $\ell_{\max}$, by

et al. [23] are substantially different at all energies. This contrasts with the clear agreement found with the work by Errea *et al.* also using the same MOCC method. Our results also disagree with the results by Igenbergs *et al.* [25] obtained using the AOCC approach across the entire energy domain. Interestingly, at high energies, the AOCC results replicate the WP-CCC ones for H(1s), substantially overestimating the H(2s) results. The reason for such a big deviation in the results from the two similar semiclassical approaches remains to be understood. We find reasonable agreement with both the
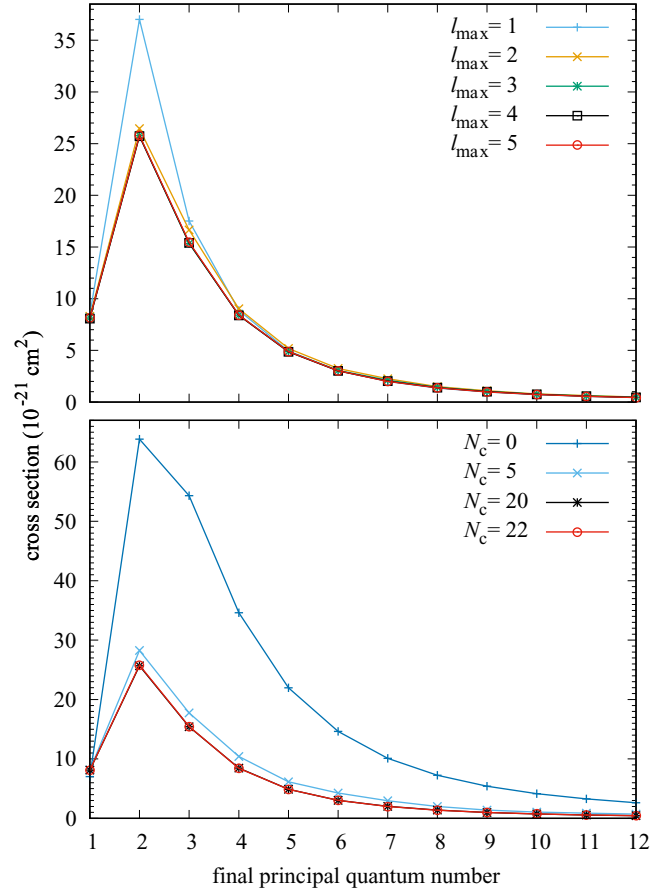
FIG. 14. *n*-partial electron-capture cross sections for Be^{4+}-H($2p_0$) collisions at projectile energy of 500 keV/u: convergence of the WP-CCC results with respect to $\ell_{\max}$ (top panel) and N_c (bottom panel) of the basis states included in the expansion.
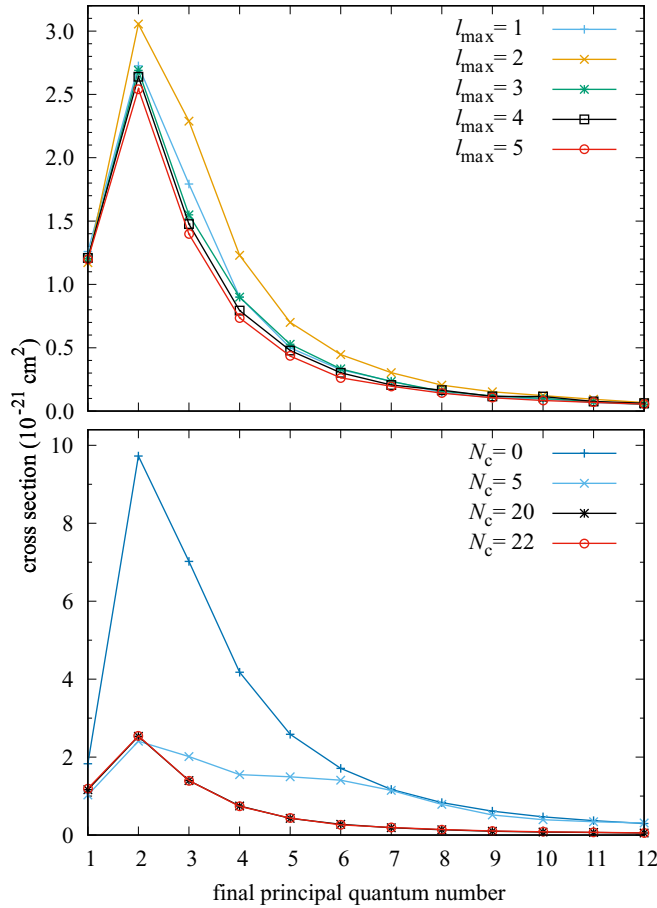

FIG. 15. *n*-partial electron-capture cross sections for Be^{4+}-H($2p_1$) collisions at projectile energy of 500 keV/u: convergence of the WP-CCC results with respect to $\ell_{\max}$ (top panel) and N_c (bottom panel) of the basis states included in the expansion.

setting $N_c = 10$ constant. One can see in the respective upper panels of Figs. 5–7 systematic convergence in all *n*-partial EC cross sections with increasing $\ell_{\max}$. It is found that for $n \leqslant 10$, setting $\ell_{\max} = 9$ produces converged results within 2% or better when scattering on all $2\ell m$ states of H. For capture from the $2s$ into states with $n \geqslant 10$, this level of convergence is maintained but increases up to about 5% for capture from the $2p_1$ state. However, when considering the target initially in the $2p_0$ state, as shown in Fig. 6, the level of convergence for capture into states with $n \geqslant 10$ is on the order of 8%. Due to the finite limit of $n_{\max}$, it is possible that the last few *n*-partial EC cross sections have slightly larger values to accommodate the flux that otherwise would go into states with $n > n_{\max}$.

The lower panels of Figs. 5–7 display the convergence of the *n*-partial EC cross sections with increasing N_c, the number of WP pseudostates representing the continuum. Here, we keep $\ell_{\max} = 9$ constant. Note that the positive-energy pseudostates contribute to electron capture implicitly through the coupling of channels. Comparing the results with $N_c = 0$ and $N_c = 10$, we conclude that the contribution from the continuum through the use of WP pseudostates cannot be neglected even at 20 keV/u. Note that $N_c = 0$ means no positive-energy states. We see a high degree of convergence achieved with respect to increasing the number of WP pseudostates for all
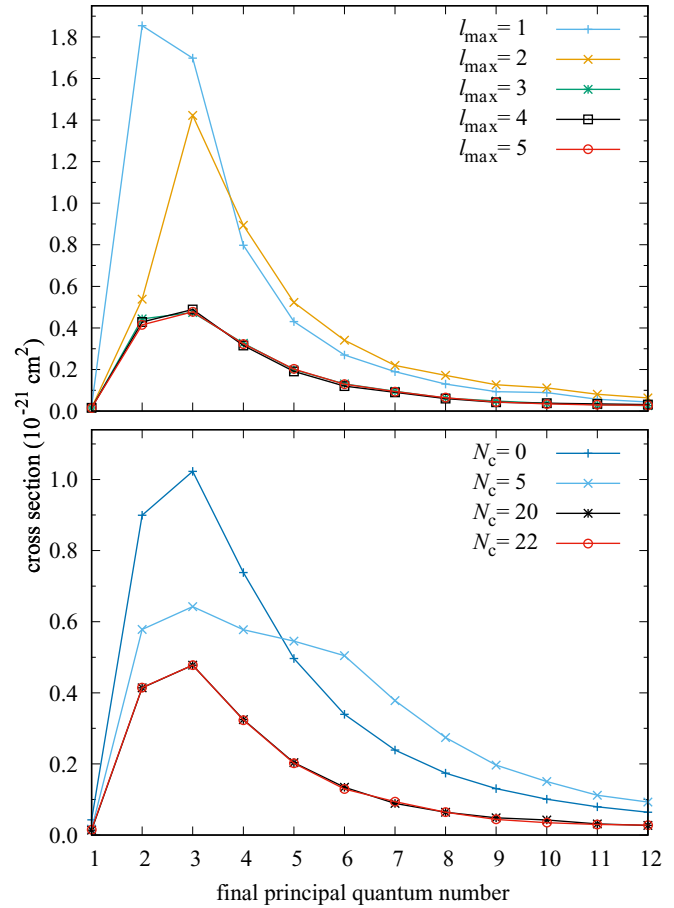
initial configurations of the target at 20 keV/u. Specifically, we reached a maximum of 1% variation in all results between setting $N_c = 8$ and $N_c = 10$.

Interesting observations can be made when looking at the relative contribution of each *n*-partial EC cross section when $\ell_{\max} = 9$ and $N_c = 10$. In particular, for capture from H($2s$) the $n = 5$ states of the Be^{3+} ion give the dominant contribution. For comparison, in our work on Be^{4+}-H($1s$) collisions, we found that at the same projectile energy, the dominant *n*-partial EC cross section was from the $n = 3$ states [19]. When the target electron initially possesses more energy in the $2\ell m$ states, we do expect the prominent *n*-resolved EC states to be higher since at low energies the transition happens into the corresponding resonance state whenever available. We also find that for collisions with hydrogen initially in the $2p_0$ and $2p_1$ states the dominant final principal quantum number for EC is $n = 7$ and $n = 6$, respectively. Thus, we find that the electron is more likely to be captured into even higher n states when the target is in the $2p_0$ and $2p_1$ states. Olson [36] suggested that in the intermediate energy regime, the dominant n state the electron is captured into is approximately given by $n \approx n_i(Z)^{3/4}$, where n_i refers to the initial principal quantum number of the hydrogen target. At 20 keV/u, we find that this relation holds for Be^{4+} collisions with H($2s$) and H($2p_1$).
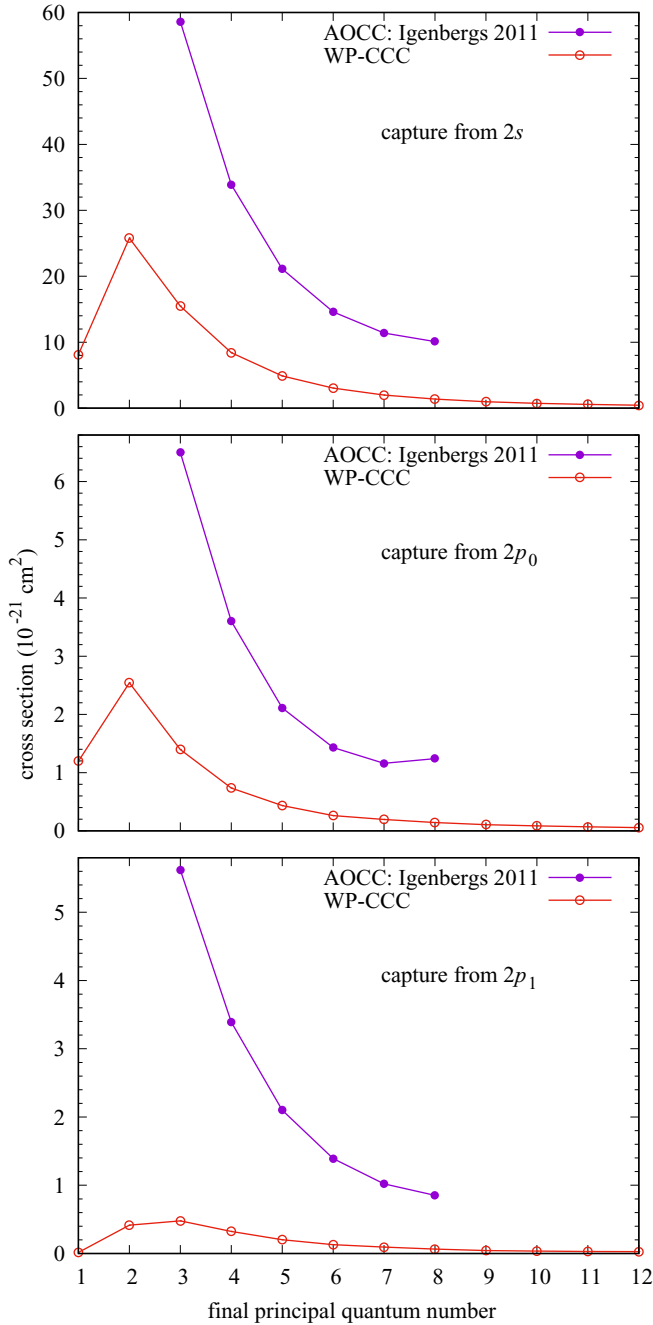
FIG. 16. *n*-partial electron-capture cross sections for Be^{4+} scattering on H(2*s*) (top panel), H(2p_0) (middle panel), and H(2p_1) (bottom panel) at projectile energy of 500 keV/u: The current WP-CCC results are shown alongside the AOCC calculations by Igenbergs [25].

However, for H(2p_0) we find the $n = 7$ state producing the dominant partial EC cross section.

Figure 8 shows the final WP-CCC *n*-partial EC cross sections at a projectile energy of 20 keV/u, in comparison with the MOCC calculations by Errea *et al.* [14] and the results obtained by Jorge *et al.* [20] using the CTMC and GTDSE approaches. The WP-CCC cross sections are in complete agreement with the CTMC and GTDSE ones but not with the MOCC calculations. Also, the MOCC results suggest the dominant *n*-partial EC cross section occurs at $n = 8$.
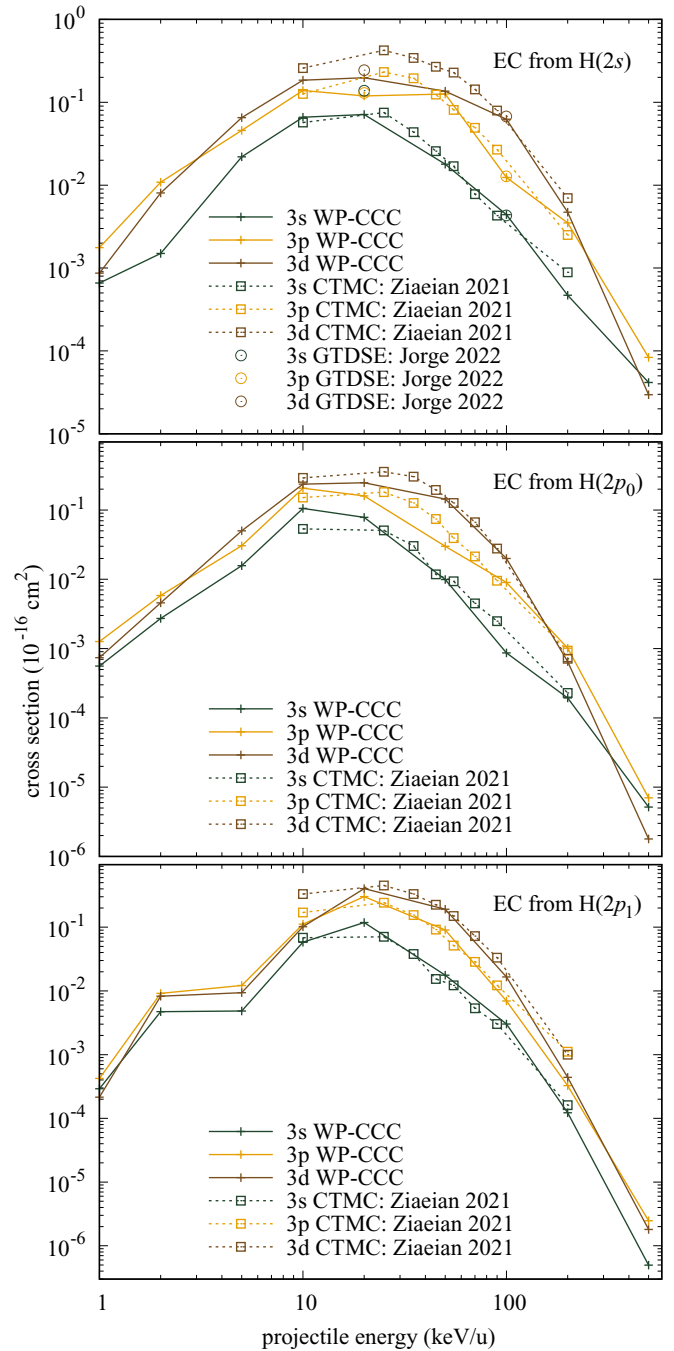
FIG. 17. 3ℓ-partial cross sections for electron capture in Be^{4+} collisions with H(2*s*) (top panel), H(2p_0) (middle panel), and H(2p_1) (bottom panel): The current WP-CCC results are shown alongside the CTMC calculations by Ziaeian and Tökési [21] and GTDSE results by Jorge *et al.* [20].

However, it is worth noting that the MOCC approach is only applicable at low incident energies, and 20 keV/u could be too high.

Figures 9–11 present the *n*-partial EC cross sections at a projectile energy of 100 keV/u. Again, we check convergence like we did at 20 keV/u but with n_{max} now set to 16. First we increase ℓ_{max}, taking $N_c = 16$. The results are shown in the upper panels. For all *n*-partial EC cross sections across the three figures, one can see excellent convergence with
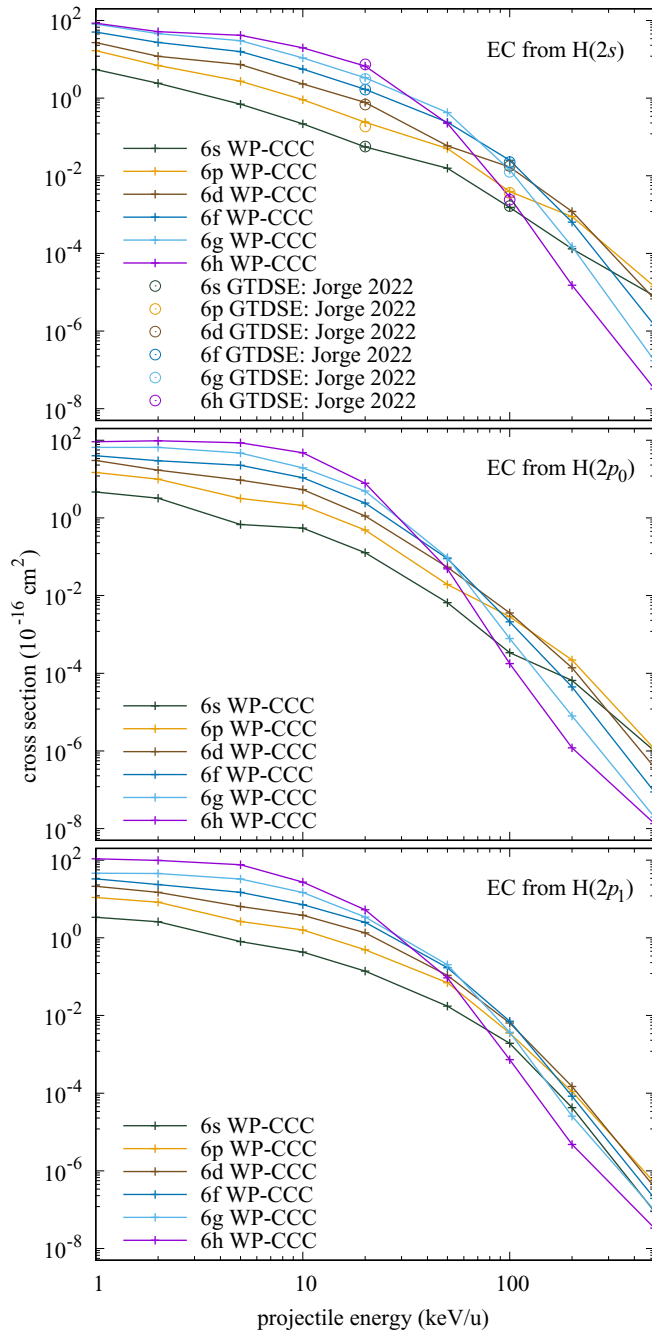
FIG. 18. 6ℓ-partial cross sections for electron capture in Be^{4+} collisions with $H(2s)$ (top panel), $H(2p_0)$ (middle panel), and $H(2p_1)$ (bottom panel): The current WP-CCC results are shown alongside the GTDSE calculations by Jorge *et al.* [20].

increasing ℓ_{max}. At this projectile energy, we find that setting $\ell_{max} = 7$ is more than sufficient to reach convergence in contrast to $\ell_{max} = 9$ required at 20 keV/u. Specifically, increasing ℓ_{max} from 6 to 7 varies the results by a maximum of 1% for collisions with all $2\ell m$ states of H at this energy. Keeping $\ell_{max} = 7$, we observe changes to the results caused by increasing the number of WP pseudostates included in the calculations. We find good convergence with respect to increasing N_c as shown in the lower panels of Figs. 9–11. That is, setting $N_c = 16$ is more than sufficient to obtain accu-

rate n-partial cross sections for EC from $H(2s)$, $H(2p_0)$, and $H(2p_1)$. Also, we find that at a projectile energy of 100 keV/u, the results have a greater dependence on N_c as compared to calculations made at 20 keV/u. This can be seen through the large variation in the results with $N_c = 0$ and $N_c = 16$.

In Fig. 12, we compare the n-partial EC cross sections at 100 keV/u with previous calculations. For capture from $H(2s)$ (top panel), our results again agree very well with the GTDSE and CTMC results by Jorge *et al.* [20] for all n. However, there is significant disagreement with the AOCC calculations by Igenbergs [25] for capture from all three of the considered initially excited states of the target. In terms of the distribution of the n-partial EC cross sections, the AOCC calculations also display unphysical peaks at $n = 8$, where we expect the results to be steadily declining. The AOCC calculations use an asymmetric basis on both centers where only eight hydrogen states are included. In our convergence studies, we apply a symmetric basis expansion; however, we also tested an asymmetric approach to investigate the contribution the target centered states have on the n-partial EC cross sections. Our analysis showed that a large and nearly symmetric basis expansion is required to obtain stable state-selective EC cross sections.

Similar convergence studies have been performed at 500 keV/u. Figures 13–15 show the convergence with increasing ℓ_{max} (top panel) and N_c (bottom panel). Here, the major difficulty in the calculations lies in the evaluation of the exchange and overlap matrix elements [19]. These particular matrix elements contain an oscillatory factor inside the integrand that depends on projectile speed. Hence, at sufficiently high energies such as 500 keV/u, a large number of Gauss-Legendre and Gauss-Laguerre points are required to ensure an accurate integration is achieved. This increase in integration points drastically extends the computational time of the results. Nevertheless, we ensure enough points are included such that there is negligible change to the results. The top panels of Figs. 13–15 show the convergence of the n-partial EC cross sections with increasing ℓ_{max}. These calculations are performed by setting $n_{max} = 12$ and $N_c = 22$. For the target initially in the $2s$ and $2p_1$ states, our results converged to within 2% or better. However, for collisions with $H(2p_0)$ the degree of convergence with increasing ℓ_{max} was slightly less. Specifically, the results with $\ell_{max} = 4$ and $\ell_{max} = 5$ for $H(2p_0)$ differ by a maximum of 5%. With ℓ_{max} set to 5, we also check the dependence of the n-partial EC cross sections on N_c. The results are shown in the lower panels of Figs. 13–15. Here, we find that the difference in the results with $N_c = 20$ and $N_c = 22$ is only marginally different for scattering on all $2\ell m$ states of H. In other words, the calculations with the two aforementioned values of N_c appear to be almost indistinguishable in the figures. By looking at the final number of WP pseudostates included to obtain converged results at 20, 100, and 500 keV/u, we find that as the projectile energy increases N_c needs to be increased. This is because in the high-energy domain, the dominant channels are ionization and target excitation. Due to the coupling between all channels, in order to obtain converged EC cross sections in the high-energy domain, we need to discretize a larger portion of the continuum. We intend to publish comprehensive studies of ionization and target excitation processes in Be^{4+}-$H(2\ell m)$ collisions elsewhere.

TABLE I. Partial $n\ell$-resolved electron-capture cross sections (in 10^{-16} cm^2) for Be^{4+}-H(2s) collisions. Notation: $a[\pm n]$ implies $a \times 10^{\pm n}$.

Be$^{3+}(n\ell)$	1	2	5	10	20	50	100	200	500
				Projectile energy (keV/u)					
$3s$	6.59[−4]	1.50[−3]	2.20[−2]	6.61[−2]	7.12[−2]	1.79[−2]	4.40[−3]	4.70[−4]	4.15[−5]
$3p$	1.77[−3]	1.08[−2]	4.58[−2]	1.39[−1]	1.19[−1]	1.26[−1]	1.24[−2]	3.50[−3]	8.35[−5]
$3d$	8.68[−4]	8.06[−3]	6.52[−2]	1.85[−1]	1.98[−1]	1.36[−1]	6.25[−2]	4.71[−3]	2.96[−5]
$4s$	1.17[−1]	3.47[−1]	4.26[−1]	7.81[−1]	1.44[−1]	2.12[−2]	3.41[−3]	3.07[−4]	2.23[−5]
$4p$	8.32[−1]	1.63[+0]	1.26[+0]	2.91[+0]	7.65[−1]	1.07[−1]	8.50[−3]	2.16[−3]	4.15[−5]
$4d$	2.62[−1]	8.90[−1]	1.32[+0]	4.62[+0]	2.82[+0]	1.03[−1]	3.69[−2]	2.97[−3]	1.81[−5]
$4f$	6.52[−1]	1.19[+0]	2.12[+0]	4.04[+0]	3.59[+0]	7.07[−1]	4.90[−2]	1.12[−3]	2.38[−6]
$5s$	2.20[+0]	3.15[+0]	1.28[+0]	2.63[−1]	8.93[−2]	1.92[−2]	2.31[−3]	2.01[−4]	1.29[−5]
$5p$	7.28[+0]	9.29[+0]	5.83[+0]	1.68[+0]	4.05[−1]	7.55[−2]	5.63[−3]	1.35[−3]	2.31[−5]
$5d$	1.47[+1]	1.98[+1]	1.66[+1]	5.61[+0]	1.34[+0]	7.78[−2]	2.46[−2]	1.85[−3]	1.07[−5]
$5f$	2.18[+1]	2.51[+1]	3.09[+1]	1.62[+1]	2.92[+0]	3.64[−1]	3.59[−2]	9.06[−4]	1.92[−6]
$5g$	2.10[+1]	2.48[+1]	3.17[+1]	2.63[+1]	1.04[+1]	5.94[−1]	1.50[−2]	1.49[−4]	1.95[−7]
$6s$	5.45[+0]	2.41[+0]	6.98[−1]	2.16[−1]	5.54[−2]	1.57[−2]	1.53[−3]	1.31[−4]	7.99[−6]
$6p$	1.67[+1]	6.92[+0]	2.70[+0]	9.08[−1]	2.40[−1]	5.04[−2]	3.93[−3]	8.88[−4]	1.40[−5]
$6d$	2.70[+1]	1.19[+1]	7.32[+0]	2.32[+0]	7.75[−1]	5.90[−2]	1.68[−2]	1.21[−3]	6.72[−6]
$6f$	5.01[+1]	2.71[+1]	1.57[+1]	5.56[+0]	1.68[+0]	2.40[−1]	2.51[−2]	6.40[−4]	1.41[−6]
$6g$	8.03[+1]	4.56[+1]	3.00[+1]	1.08[+1]	3.34[+0]	4.24[−1]	1.40[−2]	1.50[−4]	1.72[−7]
$6h$	8.49[+1]	5.13[+1]	4.14[+1]	1.98[+1]	6.71[+0]	2.24[−1]	2.79[−3]	1.51[−5]	3.23[−8]
$7s$	6.24[−1]	1.35[+0]	4.42[−1]	2.31[−1]	4.65[−2]	1.25[−2]	1.03[−3]	9.40[−5]	5.26[−6]
$7p$	1.97[+0]	3.29[+0]	1.58[+0]	8.61[−1]	1.85[−1]	3.43[−2]	2.76[−3]	5.84[−4]	9.16[−6]
$7d$	3.10[+0]	5.11[+0]	3.77[+0]	2.10[+0]	5.55[−1]	4.64[−2]	1.18[−2]	8.04[−4]	4.39[−6]
$7f$	4.41[+0]	9.13[+0]	6.68[+0]	4.22[+0]	1.29[+0]	1.69[−1]	1.76[−2]	4.68[−4]	9.52[−7]
$7g$	7.44[+0]	1.02[+1]	1.21[+1]	7.16[+0]	2.12[+0]	2.92[−1]	1.12[−2]	1.26[−4]	1.55[−7]
$7h$	1.13[+1]	1.62[+1]	2.15[+1]	1.06[+1]	2.91[+0]	2.06[−1]	3.31[−3]	1.92[−5]	3.97[−8]
$7i$	6.27[+0]	2.76[+1]	2.96[+1]	6.90[+0]	2.14[+0]	5.65[−2]	4.02[−4]	1.85[−6]	–
$8s$	2.55[−1]	3.06[−1]	2.31[−1]	2.54[−1]	3.95[−2]	1.00[−2]	6.99[−4]	6.47[−5]	3.61[−6]
$8p$	8.19[−1]	7.11[−1]	8.31[−1]	7.75[−1]	1.52[−1]	2.42[−2]	2.04[−3]	4.43[−4]	6.14[−6]
$8d$	1.55[+0]	1.06[+0]	1.84[+0]	2.04[+0]	4.38[−1]	3.74[−2]	8.45[−3]	5.51[−4]	3.10[−6]
$8f$	3.02[+0]	1.68[+0]	3.40[+0]	3.23[+0]	1.04[+0]	1.22[−1]	1.29[−2]	3.31[−4]	7.39[−7]
$8g$	4.65[+0]	1.88[+0]	5.48[+0]	5.58[+0]	1.55[+0]	2.05[−1]	8.64[−3]	1.08[−4]	1.10[−7]
$8h$	5.41[+0]	4.14[+0]	7.55[+0]	7.49[+0]	1.62[+0]	1.62[−1]	3.03[−3]	2.09[−5]	5.67[−8]
$8i$	4.01[+0]	5.57[+0]	8.09[+0]	5.20[+0]	1.25[+0]	6.37[−2]	5.69[−4]	4.54[−6]	–
$8k$	1.21[+0]	3.53[+0]	6.39[+0]	2.03[+0]	5.07[−1]	9.82[−3]	4.88[−5]	2.35[−6]	–

Figure 16 presents the WP-CCC results for the n-partial EC cross sections with the final basis paramaters $n_{\max} = 12$, $\ell_{\max} = 5$, and $N_c = 22$ at 500 keV/u. The results are compared with the calculations by Igenbergs [25] using the AOCC approach. Similar to the 100-keV/u case presented in Fig. 12, we find large discrepancies between the two results. Specifically, the minimum difference between our two sets of results is 92%. More calculations using alternative methods would help resolve the discrepancy.

Throughout this section, we have presented convergence tests on n-partial EC cross sections at three key impact energies: 20, 100, and 500 keV/u. These energies provide a good indication of the basis parameters required to obtain accurate state-selective cross sections at low, intermediate, and high energy regions. At 20 keV/u, we find the minimum necessary size of the two-center basis to be 4770 states whereas at 100 and 500 keV/u the required basis size decreases to 3480 and 2198 states, respectively. This indicates that as the projectile energy increases, the basis size can be reduced. Nevertheless, in comparison with the size of the basis needed for Be^{4+}-H(1s) collisions [19], a significantly larger basis

is needed for collisions with H($2\ell m$). This agrees with the observations made in Ref. [34] where p-H($2\ell m$) collisions were studied.

D. $n\ell$-resolved cross sections

Figures 17 and 18 display the energy dependence of the calculated 3ℓ- and 6ℓ-partial EC cross sections, respectively. The top, middle, and lower panels in each figure contain the results for capture from H(2s), H($2p_0$), and H($2p_1$), respectively. Furthermore, results for 4ℓ-, 5ℓ-, 7ℓ-, and 8ℓ-partial cross sections can be found in Tables I–III. The largest cross sections are convergent within a few percent; however, the smallest ones are converged only within ≈8%. Through analysis of Figs. 17 and 18, along with the data supplied in the tables, we can make the following observations. Within each set of results for the 3ℓ- to 5ℓ-partial EC cross sections, in the energy region between 5 and 50 keV/u, the dominant $n\ell$ state for capture is the one with the largest allowed ℓ within the shell, i.e., $\ell = n - 1$. In the same energy region, in the 6ℓ- to 8ℓ-partial cross sections, dominant contributions

TABLE II. Partial $n\ell$-resolved electron-capture cross sections (in 10^{-16} cm^2) for Be^{4+}-H($2p_0$) collisions. Notation: $a[\pm n]$ implies $a \times 10^{\pm n}$.

				Projectile energy (keV/u)					
Be^{3+}($n\ell$)	1	2	5	10	20	50	100	200	500
3s	5.60[−4]	2.72[−3]	1.57[−2]	1.05[−1]	7.82[−2]	9.91[−3]	8.67[−4]	1.93[−4]	5.17[−6]
3p	1.26[−3]	5.84[−3]	3.04[−2]	2.06[−1]	1.59[−1]	3.00[−2]	8.98[−3]	1.01[−3]	7.01[−6]
3d	7.38[−4]	4.57[−3]	5.01[−2]	2.36[−1]	2.47[−1]	1.44[−1]	2.00[−2]	6.49[−4]	1.79[−6]
4s	8.02[−2]	2.66[−1]	4.78[−1]	2.43[−1]	7.55[−2]	8.17[−3]	5.24[−4]	1.38[−4]	2.72[−6]
4p	6.42[−1]	1.22[+0]	1.55[+0]	8.03[−1]	2.48[−1]	1.64[−2]	5.89[−3]	5.74[−4]	3.42[−6]
4d	1.72[−1]	8.06[−1]	1.92[+0]	1.35[+0]	4.94[−1]	5.84[−2]	9.50[−3]	3.67[−4]	1.03[−6]
4f	5.07[−1]	1.51[+0]	2.76[+0]	2.63[+0]	1.28[+0]	7.30[−2]	4.28[−3]	8.19[−5]	1.73[−7]
5s	1.94[+0]	1.51[+0]	8.85[−1]	4.94[−1]	1.14[−1]	7.35[−3]	3.90[−4]	9.37[−5]	1.63[−6]
5p	1.15[+1]	5.92[+0]	3.61[+0]	1.70[+0]	4.28[−1]	1.85[−2]	3.99[−3]	3.47[−4]	1.96[−6]
5d	1.44[+1]	1.65[+1]	9.30[+0]	4.40[+0]	9.27[−1]	5.66[−2]	5.46[−3]	2.20[−4]	6.15[−7]
5f	1.84[+1]	2.24[+1]	1.79[+1]	1.08[+1]	2.28[+0]	8.37[−2]	2.98[−3]	6.36[−5]	1.16[−7]
5g	1.72[+1]	2.32[+1]	2.39[+1]	2.33[+1]	6.06[+0]	7.43[−2]	7.80[−4]	8.09[−6]	2.69[−8]
6s	4.64[+0]	3.21[+0]	6.78[−1]	5.45[−1]	1.27[−1]	6.58[−3]	3.39[−4]	6.55[−5]	9.96[−7]
6p	1.48[+1]	9.93[+0]	3.16[+0]	2.09[+0]	4.88[−1]	1.93[−2]	2.85[−3]	2.20[−4]	1.13[−6]
6d	3.00[+1]	1.70[+1]	9.39[+0]	5.36[+0]	1.11[+0]	5.39[−2]	3.56[−3]	1.38[−4]	3.78[−7]
6f	3.99[+1]	2.95[+1]	2.25[+1]	1.08[+1]	2.41[+0]	8.94[−2]	2.12[−3]	4.46[−5]	8.79[−8]
6g	6.53[+1]	6.55[+1]	4.67[+1]	1.94[+1]	4.89[+0]	9.54[−2]	7.84[−4]	7.95[−6]	1.98[−8]
6h	9.13[+1]	9.67[+1]	8.58[+1]	4.75[+1]	7.79[+0]	4.90[−2]	1.78[−4]	1.20[−6]	1.35[−8]
7s	8.83[−1]	9.41[−1]	2.67[−1]	3.03[−1]	1.11[−1]	5.64[−3]	2.64[−4]	4.51[−5]	7.00[−7]
7p	3.35[+0]	2.15[+0]	1.10[+0]	1.20[+0]	4.16[−1]	1.76[−2]	2.04[−3]	1.50[−4]	8.22[−7]
7d	5.96[+0]	3.37[+0]	3.07[+0]	3.13[+0]	9.65[−1]	4.83[−2]	2.49[−3]	9.17[−5]	2.80[−7]
7f	5.73[+0]	5.83[+0]	7.06[+0]	6.31[+0]	1.95[+0]	8.19[−2]	1.61[−3]	3.05[−5]	7.72[−8]
7g	5.12[+0]	1.12[+1]	1.34[+1]	9.38[+0]	3.65[+0]	9.27[−2]	7.07[−4]	6.77[−6]	3.93[−8]
7h	9.22[+0]	1.06[+1]	2.01[+1]	1.48[+1]	6.02[+0]	6.04[−2]	2.20[−4]	1.78[−6]	3.79[−8]
7i	8.97[+0]	2.06[+1]	3.42[+1]	2.86[+1]	4.42[+0]	1.74[−2]	3.19[−5]	4.86[−7]	−
8s	2.96[−1]	1.44[−1]	1.25[−1]	1.40[−1]	8.63[−2]	4.67[−3]	2.14[−4]	3.10[−5]	5.09[−7]
8p	8.99[−1]	3.91[−1]	4.45[−1]	6.69[−1]	3.45[−1]	1.41[−2]	1.59[−3]	1.04[−4]	5.89[−7]
8d	1.69[+0]	6.86[−1]	1.11[+0]	1.60[+0]	7.59[−1]	3.98[−2]	1.89[−3]	6.98[−5]	2.01[−7]
8f	3.44[+0]	1.21[+0]	2.09[+0]	3.37[+0]	1.51[+0]	7.07[−2]	1.17[−3]	2.50[−5]	5.77[−8]
8g	4.90[+0]	1.70[+0]	3.76[+0]	4.29[+0]	2.73[+0]	7.97[−2]	5.77[−4]	6.18[−6]	2.40[−8]
8h	5.45[+0]	4.04[+0]	4.74[+0]	5.84[+0]	4.30[+0]	5.70[−2]	2.18[−4]	2.67[−6]	3.25[−8]
8i	3.32[+0]	6.39[+0]	4.11[+0]	1.03[+1]	4.09[+0]	2.28[−2]	4.56[−5]	2.33[−6]	−
8k	1.12[+0]	3.57[+0]	3.52[+0]	9.20[+0]	1.56[+0]	3.56[−3]	7.31[−6]	1.40[−6]	−

comes from capture into the state with $\ell \approx Z^{3/4}$. This is in agreement with the findings of Olson [36]. Note that the 7ℓ- and 8ℓ-resolved EC cross sections in Tables I–III do not show the results for the partial $7i$, $8i$, and $8k$ cross sections at 500 keV/u. As discussed in Sec. III C, the largest ℓ_{max} was 5. Hence the aforementioned states are not included in the calculations.

In Figs. 17 and 18, we compare our 3ℓ- and 6ℓ-partial EC cross sections to previous calculations. For capture from H($2p_0$) and H($2p_1$), the WP-CCC results for the 3ℓ-partial cross sections appear to agree reasonably well with the CTMC results by Ziaeian and Tökési [21] across the majority of the overlapping energy range. However, we do notice significant discrepancies when comparing our $3d$-partial cross sections from H($2s$) to the CTMC ones below 100 keV/u. As also seen in Figs. 17 and 18, for capture from H($2s$), our 3ℓ- and 6ℓ-partial cross sections show excellent agreement with the GTDSE calculations by Jorge *et al.* [20] at the two projectiles energies reported in their work. This is excluding the results for capture into the $3s$ state at 20 keV/u, where we find noticeable differences between our results.

IV. CONCLUSIONS

The wave-packet convergent close-coupling approach is applied to model electron capture processes in Be^{4+} ion collisions with atomic hydrogen initially in the $2s$, $2p_0$, and $2p_1$ excited states. We present integrated total, n-, and $n\ell$-resolved electron-capture cross sections required for plasma impurity diagnostics. These results are calculated in a broad projectile energy range between 1 and 500 keV/u. To ensure the accuracy of our results, we have performed thorough convergence studies with regards to the number of basis states included in the expansion of the total scattering wave function. The states we use to construct the basis consists of true negative-energy eigenstates and wave-packet pseudostates about each center. Our results show that below projectile energies of 40 keV/u, capture from the hydrogen target initially in the $2\ell m$ excited states produces a significantly larger total cross section in comparison to capture from H($1s$). However, above 40 keV/u, electron capture is more likely to occur when the target is in the ground state. To date, there is no experimental data for this collision system. Therefore, calculated cross sections have been compared solely with previous

TABLE III. Partial $n\ell$-resolved electron-capture cross sections (in 10^{-16} cm^2) for Be^{4+}-H($2p_1$) collisions. Notation: $a[\pm n]$ implies $a \times 10^{\pm n}$.

Be^{3+}($n\ell$)	Projectile energy (keV/u)								
	1	2	5	10	20	50	100	200	500
3s	2.92[−4]	4.73[−3]	4.84[−3]	5.80[−2]	1.19[−1]	1.77[−2]	3.02[−3]	1.22[−4]	4.97[−7]
3p	4.23[−4]	9.16[−3]	1.22[−2]	1.11[−1]	3.01[−1]	9.06[−2]	6.95[−3]	3.25[−4]	2.48[−6]
3d	2.15[−4]	8.27[−3]	9.38[−3]	1.02[−1]	4.02[−1]	1.91[−1]	1.66[−2]	4.40[−4]	1.80[−6]
4s	9.07[−2]	3.37[−1]	7.62[−1]	6.54[−1]	1.65[−1]	2.12[−2]	3.11[−3]	9.10[−5]	2.67[−7]
4p	1.69[−1]	4.85[−1]	1.90[+0]	2.25[+0]	6.74[−1]	9.83[−2]	6.51[−3]	2.32[−4]	1.38[−6]
4d	3.89[−1]	1.23[+0]	2.72[+0]	3.64[+0]	2.16[+0]	1.65[−1]	1.22[−2]	3.29[−4]	1.04[−6]
4f	2.36[−1]	5.72[−1]	2.60[+0]	4.69[+0]	3.62[+0]	3.65[−1]	1.24[−2]	1.44[−4]	5.45[−7]
5s	2.64[+0]	3.40[+0]	1.36[+0]	6.78[−1]	1.60[−1]	2.00[−2]	2.51[−3]	5.94[−5]	1.55[−7]
5p	7.37[+0]	1.05[+1]	5.54[+0]	2.34[+0]	5.87[−1]	8.75[−2]	4.91[−3]	1.55[−4]	8.02[−7]
5d	1.24[+1]	1.52[+1]	1.17[+1]	5.70[+0]	1.62[+0]	1.39[−1]	8.90[−3]	2.21[−4]	6.09[−7]
5f	2.00[+1]	2.42[+1]	2.08[+1]	1.31[+1]	3.23[+0]	2.36[−1]	9.75[−3]	1.17[−4]	3.05[−7]
5g	2.86[+1]	3.50[+1]	3.73[+1]	2.48[+1]	6.22[+0]	2.51[−1]	3.81[−3]	2.84[−5]	1.47[−7]
6s	3.36[+0]	2.58[+0]	8.00[−1]	4.28[−1]	1.39[−1]	1.73[−2]	1.92[−3]	4.23[−5]	9.06[−8]
6p	1.09[+1]	8.22[+0]	2.62[+0]	1.60[+0]	4.92[−1]	7.02[−2]	3.53[−3]	1.09[−4]	4.98[−7]
6d	2.12[+1]	1.48[+1]	6.36[+0]	3.79[+0]	1.35[+0]	1.08[−1]	6.40[−3]	1.49[−4]	3.82[−7]
6f	3.28[+1]	2.34[+1]	1.48[+1]	7.12[+0]	2.51[+0]	1.70[−1]	7.10[−3]	8.38[−5]	1.95[−7]
6g	4.59[+1]	4.51[+1]	3.25[+1]	1.47[+1]	3.41[+0]	2.02[−1]	3.70[−3]	2.55[−5]	9.71[−8]
6h	1.08[+2]	9.79[+1]	7.63[+1]	2.71[+1]	5.27[+0]	9.31[−2]	7.32[−4]	4.80[−6]	3.34[−8]
7s	5.61[−1]	4.22[−1]	3.59[−1]	3.00[−1]	1.10[−1]	1.42[−2]	1.42[−3]	2.88[−5]	6.17[−8]
7p	1.97[+0]	1.50[+0]	1.31[+0]	1.04[+0]	3.94[−1]	5.40[−2]	2.58[−3]	7.48[−5]	3.35[−7]
7d	3.59[+0]	3.10[+0]	2.83[+0]	2.39[+0]	1.06[+0]	8.14[−2]	4.62[−3]	1.10[−4]	2.74[−7]
7f	6.55[+0]	5.17[+0]	5.36[+0]	4.26[+0]	1.87[+0]	1.27[−1]	5.18[−3]	6.56[−5]	1.46[−7]
7g	1.10[+1]	7.99[+0]	1.04[+1]	8.21[+0]	2.49[+0]	1.53[−1]	3.05[−3]	2.08[−5]	8.51[−8]
7h	1.11[+1]	1.56[+1]	1.82[+1]	1.29[+1]	3.55[+0]	9.42[−2]	8.79[−4]	5.23[−6]	3.59[−8]
7i	8.68[+0]	2.20[+1]	3.14[+1]	1.58[+1]	2.55[+0]	2.40[−2]	1.09[−4]	9.80[−7]	–
8s	1.05[−1]	1.42[−1]	1.93[−1]	2.03[−1]	8.69[−2]	1.16[−2]	1.08[−3]	1.90[−5]	4.27[−8]
8p	2.91[−1]	3.67[−1]	6.39[−1]	7.37[−1]	3.12[−1]	4.18[−2]	1.89[−3]	5.17[−5]	2.21[−7]
8d	4.72[−1]	6.36[−1]	1.22[+0]	1.50[+0]	8.29[−1]	6.20[−2]	3.46[−3]	6.67[−5]	1.69[−7]
8f	6.98[−1]	7.44[−1]	2.36[+0]	2.73[+0]	1.40[+0]	9.49[−2]	3.75[−3]	4.09[−5]	9.42[−8]
8g	1.02[+0]	1.18[+0]	3.62[+0]	4.86[+0]	1.89[+0]	1.15[−1]	2.37[−3]	2.09[−5]	5.36[−8]
8h	1.11[+0]	1.43[+0]	4.66[+0]	6.98[+0]	2.56[+0]	7.93[−2]	8.35[−4]	8.26[−6]	6.24[−8]
8i	1.09[+0]	1.48[+0]	5.81[+0]	8.59[+0]	2.25[+0]	2.87[−2]	1.52[−4]	3.43[−6]	–
8k	4.53[−1]	1.54[+0]	5.09[+0]	5.79[+0]	8.37[−1]	4.24[−3]	1.39[−5]	1.59[−6]	–

theoretical calculations where available. Our results for the total and state-selective electron capture cross sections significantly differ from those previously obtained using the AOCC approach across the entire energy domain. However, good agreement is seen with the recent calculations using a CTMC and GTDSE method where available. Arguably, this work addresses the concerns expressed in Refs. [20,21] with regards to the accuracy of previously conducted close-coupling calculations.

This investigation was performed within the framework of the IAEA Coordinated Research Project on Data for Atomic Processes of Neutral Beams in Fusion Plasma [37]. Data presented here can be used for diagnostics and spectroscopy of plasma containing beryllium ions. All the n- and nl-resolved

cross sections from this work, as well a comprehensive set of state-selective nlm cross sections, will be available in due course through the IAEA data repositories. In addition, all the underlying data behind this study are available from the authors upon reasonable request.

[1] O. Marchuk, Phys. Scr. **89**, 114010 (2014).

[2] R. Pitts, S. Carpentier, F. Escourbiac, T. Hirai, V. Komarov, A. Kukushkin, S. Lisgo, A. Loarte, M. Merola, R. Mitteau, A. Raffray, M. Shimada, and P. Stangeby, J. Nucl. Mater. **415**, S957 (2011).

[3] H. P. Summers, W. J. Dickson, A. Boileau, P. G. Burke, B. Denne-Hinnov, W. Fritsch, R. Giannella, N. C. Hawkes, M. von Hellerman, W. Mandl, N. J. Peacock, R. H. G. Reid, M. F. Stamp, and P. R. Thomas, Plasma Phys. Controlled Fusion **34**, 325 (1992).

[4] R. C. Isler, Plasma Phys. Controlled Fusion **36**, 171 (1994).

[5] R. C. Isler and R. E. Olson, Phys. Rev. A **37**, 3399 (1988).

[6] Dž. Belkić, S. Saini, and H. S. Taylor, Phys. Rev. A **36**, 1601 (1987).

[7] N. Stolterfoht, R. DuBois, and R. Rivarola, *Electron Emission in Heavy-Ion-Atom Collisions*, Springer Series on Atoms and Plasmas (Springer, Berlin, 1997).

[8] D. R. Schultz and P. S. Krstic, *Atomic and Plasma–Material Interaction Data for Fusion*, Vol. 6, (IAEA, Vienna, 1997), p. 173.

[9] I. Ziaeian and K. Tőkési, Atoms **8**, 27 (2020).

[10] N. Toshima, Phys. Rev. A **50**, 3940 (1994).

[11] H. Agueny, J. P. Hansen, A. Dubois, A. Makhoute, A. Taoutioui, and N. Sisourat, At. Data Nucl. Data Tables **129–130**, 101281 (2019).

[12] A. C. K. Leung and T. Kirchner, Atoms **10**, 11 (2022).

[13] C. Harel, H. Jouin, and B. Pons, At. Data Nucl. Data Tables **68**, 279 (1998).

[14] L. F. Errea, C. Harel, H. Jouin, L. Méndez, B. Pons, and A. Riera, J. Phys. B: At., Mol. Opt. Phys. **31**, 3527 (1998).

[15] T. Minami, M. S. Pindzola, T.-G. Lee, and D. R. Schultz, J. Phys. B: At., Mol. Opt. Phys. **39**, 2877 (2006).

[16] A. Jorge, J. Suárez, C. Illescas, L. F. Errea, and L. Méndez, Phys. Rev. A **94**, 032707 (2016).

[17] Dž. Belkić, I. Bray, and A. S. Kadyrov (eds.), *State-of-the-Art Reviews on Energetic Ion-Atom and Ion-Molecule Collisions* (World Scientific, Singapore, 2019).

[18] Edited by M. Schulz, *Ion-Atom Collisions: The Few-Body Problem in Dynamic Systems* (De Gruyter, Berlin, 2019).

[19] N. W. Antonio, C. T. Plowman, I. B. Abdurakhmanov, I. Bray, and A. S. Kadyrov, J. Phys. B: At., Mol. Opt. Phys. **54**, 175201 (2021).

[20] A. Jorge, C. Illescas, and L. Méndez, Phys. Rev. A **105**, 012811 (2022).

[21] I. Ziaeian and K. Tökési, Eur. Phys. J. D **75**, 138 (2021).

[22] R. Hoekstra, H. Anderson, F. W. Bliek, M. von Hellermann, C. F. Maggi, R. E. Olson, and H. P. Summers, Plasma Phys. Controlled Fusion **40**, 1541 (1998).

[23] N. Shimakura, N. Kobayashi, M. Honma, T. Nakano, and H. Kubo, J. Phys.: Conf. Ser. **163**, 012045 (2009).

[24] K. Igenbergs, J. Schweinzer, and F. Aumayr, J. Phys. B: At., Mol. Opt. Phys. **42**, 235206 (2009).

[25] K. Igenbergs, Calculations of cross sections relevant for diagnostics of hot fusion plasmas, Ph.D. thesis, Vienna University of Technology, Vienna, Austria, 2011.

[26] I. B. Abdurakhmanov, A. S. Kadyrov, and I. Bray, Phys. Rev. A **94**, 022703 (2016).

[27] I. B. Abdurakhmanov, J. J. Bailey, A. S. Kadyrov, and I. Bray, Phys. Rev. A **97**, 032707 (2018).

[28] I. B. Abdurakhmanov, O. Erkilic, A. S. Kadyrov, I. Bray, S. K. Avazbaev, and A. M. Mukhamedzhanov, J. Phys. B: At. Mol. Opt. Phys. **52**, 105701 (2019).

[29] J. Faulkner, I. B. Abdurakhmanov, S. U. Alladustov, A. S. Kadyrov, and I. Bray, Plasma Phys. Control. Fusion **61**, 095005 (2019).

[30] I. B. Abdurakhmanov, K. Massen-Hane, S. U. Alladustov, J. J. Bailey, A. S. Kadyrov, and I. Bray, Phys. Rev. A **98**, 062710 (2018).

[31] A. M. Kotian, C. T. Plowman, I. B. Abdurakhmanov, I. Bray, and A. S. Kadyrov, J. Phys. B: At., Mol. Opt. Phys. **55**, 115201 (2022).

[32] S. U. Alladustov, I. B. Abdurakhmanov, A. S. Kadyrov, I. Bray, and K. Bartschat, Phys. Rev. A **99**, 052706 (2019).

[33] C. T. Plowman, I. B. Abdurakhmanov, I. Bray, and A. S. Kadyrov, Eur. Phys. J. D **76**, 31 (2022).

[34] I. B. Abdurakhmanov, S. U. Alladustov, J. J. Bailey, A. S. Kadyrov, and I. Bray, Plasma Phys. Controlled Fusion **60**, 095009 (2018).

[35] I. B. Abdurakhmanov, A. S. Kadyrov, S. K. Avazbaev, and I. Bray, J. Phys. B: At. Mol. Opt. Phys. **49**, 115203 (2016).

[36] R. E. Olson, Phys. Rev. A **24**, 1726 (1981).

[37] IAEA Coordinated Research Project, Data for Atomic Processes of Neutral Beams in Fusion Plasma, https://amdis.iaea.org/CRP/neutral-beams.